Heterostructured PHI-PTI/Li⁺Cl⁻ Carbon Nitrides for Multiple Photocatalytic Applications

Alexey Galushchinskiy, Carolina Pulignani, Horatiu Szalad, Erwin Reisner, Josep Albero, Nadezda V. Tarakina, Christian Mark Pelicano, Hermenegildo García, Oleksandr Savateev,* and Markus Antonietti

Two series of novel carbon nitride photocatalysts, Rho-CN ("rhodizonate-doped carbon nitride") and Rho-CN-TC (Rho-CN treated in potassium thiocyanate melt), are synthesized in a multistep fashion via copolymerization of cyanamide with potassium rhodizonate. The formed ionic carbon nitrides are composed of poly(triazine imide) (PTI/Li⁺Cl⁻) and potassium poly(heptazine imide) (K-PHI) phases and provide a broad absorption range up to 800 nm. The photocatalysts are characterized by several techniques (including diffuse reflectance ultraviolet–visible, powder X-ray diffraction, Fourier transform infrared, scanning electron microscopy, and electrochemical methods) and studied in a series of photocatalytic reactions, including red light-promoted benzylamine oxidation, dual photoredox/nickel C–N cross-coupling, and hydrogen peroxide evolution. The optimal ratio of rhodizonate dopant in its mixture with cyanamide is found to be 0.5 mol%. The performance of the newly synthesized materials is comparable to the activities of the benchmark catalysts K-PHI and CN-OA-m (defective poly(heptazine imide) doped with oxamide), while not requiring more expensive nitrogen sources for preparation, like 5-aminotetrazole, or multiple oven cycles.

A. Galushchinskiy, N. V. Tarakina, C. M. Pelicano, O. Savateev,
M. Antonietti
Department of Colloid Chemistry
Max Planck Institute of Colloids and Interfaces
14476 Potsdam, Germany
E-mail: oleksandr.savatieiev@mpikg.mpg.de

C. Pulignani, E. Reisner
Yusuf Hamied Department of Chemistry
University of Cambridge
Cambridge CB2 1EW, UK

H. Szalad, J. Albero, H. García
Departamento de Química/Instituto Universitario de Tecnología Química
CSIC-UPV
Universitat Politècnica de València
46022 Valencia, Spain

1. Introduction

Graphitic carbon nitrides (gCNs) represent a large class of materials composed of sp^2-hybridized carbon and nitrogen in stoichiometry close to C_3N_4.[1] Within this class, materials are divided into heptazine- and triazine-based gCNs.[2] The thermodynamically most stable form of gCN is a material in which carbon and nitrogen atoms form heptazine units linked together via sp^2-hybridized bridging nitrogen atoms, whereas layers of heptazine units are attracted via van der Waals forces. gCN materials are prepared by calcination of nitrogen-rich precursors, such as urea, cyanamide, or melamine at 550–600 °C.[3] gCNs possess an onset of light absorption at ≈470 nm that corresponds to an optical gap of 2.7 eV, which is on the edge of the visible range of electromagnetic spectrum.[4] Taking into account that efficacy of gCN materials in photo(electro)catalysis depends strongly on the amount of light it harvests, it is essential to narrow the optical gap to 2.5–2 eV for potential application under real sunlight. Several strategies have been adopted to achieve this goal: substitutional doping of C and N atoms with heteroelements and vacancies;[5] formation of heterojunction between gCN and another semiconductor;[6] or formation of triazine–heptazine donor–acceptor structure.[7] Such modified carbon nitrides can be utilized as photocatalysts for hydrogen evolution,[8] pollutant degradation,[9] oxidation reactions,[10] and other complex organic transformations.[11] In addition to more traditional photocatalytic procedures, there is a number of recent reports on advanced techniques that can be achieved by modified carbon nitrides, including "dark photocatalysis" (photocharging the material in the presence of an electron donor and then performing a reductive reaction without irradiation),[12] chromoselective transformations in which the main product depends on irradiation wavelength,[13] and dual action as a proton transfer catalysts together with electron transfer due to basicity of heptazine units.[14] Therefore, research on fine-tuning of carbon nitride properties is beneficial to expand the scope of heterogeneous photocatalysts.

Here, we report co-condensation of potassium rhodizonate with cyanamide in a LiCl:KCl eutectic mixture at 550 °C to prepare a series of carbon nitride materials featuring a triazine–heptazine donor–acceptor structure. The absorption edge in these materials

is progressively shifted up to 800 nm by increasing content of potassium rhodizonate in the mixture, allowing them to carry out a set of diverse photocatalytic organic processes.

2. Results and Discussion

2.1. Synthetic Approach

We aimed in this study to create carbon nitride species, which could be prepared by copolymerization of nitrogen-rich precursor with functionalized organic dyes in the conjugated system of heptazine layers to increase the absorption in the visible range beyond 450 nm. However, the task to identify an optimal dye is not trivial as there are multiple desirable properties of the dye that require consideration. For instance, the proposed molecule should be thermally stable, but the majority of organic dyes decompose at temperatures far below 500 °C, which is the lowest temperature needed for the formation of heptazine-based carbon nitrides, such as melon.[15] In addition to thermal stability, chemical integrity of a dye should also be preserved during extended reaction time at highly elevated temperatures, as forming nucleophilic species, including ammonia, can disrupt its conjugated system. The dye should also have reactive functional groups that allow accessibility of its electronic structure to the rest of the material. Finally, the dye should preserve its absorbance in the 450–800 nm range and be easily synthesized at scale.

We selected potassium rhodizonate (K_2Rho), the dipotassium salt of 3,4,5,6-tetraoxocyclohexene-1,2-diol, which is used in niche applications related to the analysis of heavy metal content through formation of colored or insoluble complexes (e.g., in lead rapid abrasion test kits).[15,16] K_2Rho is a fairly strongly absorbing dye with an absorption maximum in the blue to green–yellow region of visible spectrum ($\varepsilon = 3.3 \cdot 10^4$ L mol^{-1} cm^{-1} at $\lambda_{max} = 483$ nm in aqueous media).[17] This gives the dye its deep, almost black, purplish-red color in bulk, and it is stable at least until 300 °C.[18] Thermogravimetric analysis experiments demonstrate 67% mass retention up until 600 °C (Figure S10, Supporting Information), and it can easily be prepared by oxidation of inositol,

which is available commercially.[19] Its conjugated system is stabilized by equal delocalization of double negative charge between carbonyl groups and provides excellent charge capacity and transfer properties.[20] However, these functionalities are also susceptible to reaction with nucleophiles while preserving its electronic structure.[21] As a reactive nitrogen-rich compound and a copolymerization coupling partner for K_2Rho, we chose cyanamide, which is a known cheap bulk precursor to mesoporous carbon nitrides.[22] Additionally, cyanamide has strongly nucleophilic nitrogen atoms which can react with carbonyl groups of K_2Rho and, unlike most aliphatic and (hetero)aromatic amines, is weakly acidic with a pK_a of 10.3,[23] which is crucial as K_2Rho tends to decompose rapidly in basic media.[17] Finally, the viability of our synthetic strategy is supported by the fact that cyclohexanehexone, a compound structurally similar to K_2Rho, was successfully applied in the synthesis of C_2N materials by polycondensation with urea at 500 °C.[24]

The synthesis of the materials was performed in two steps (**Figure 1**a) by first co-evaporating an aqueous solution of cyanamide and K_2Rho mixture at 60 °C with a rhodizonate molar fraction ranging from 0.25% to 1%, giving a nonhomogeneous beige to brown–green or dark brown solid mass. This intermediate material, prepolymer, was not characterized further but it is suspected to be a solid gel network of cyanamide oligomers linker by rhodizonate units, possibly containing unreacted starting materials and/or dicyandiamide.[24] The prepolymer was then mixed with eutectic (K,Li)Cl mixture in a ball mill and annealed at 550 °C under nitrogen; the final materials, Rho-CN-0.25, Rho-CN-0.5, and Rho-CN-1 ("Rho-CN" stands for "rhodizonate-doped carbon nitride;" numbers indicate molar percentage of K_2Rho in the starting mixture), were obtained by washing out the salt template from the formed solid in high yields (up to 65% retention of combined organic mass). In an attempt to further increase the content of anionic fractions and introduce cyanimide groups, which facilitate transfer of photogenerated electrons to the reagents or cocatalyst,[25] the Rho-CN materials were additionally treated in potassium thiocyanate (KSCN) melt as described in the literature, producing three corresponding Rho-CN-TC catalysts ("TC" refers to "ThioCyanate") (Figure 1b).[26] The six catalysts
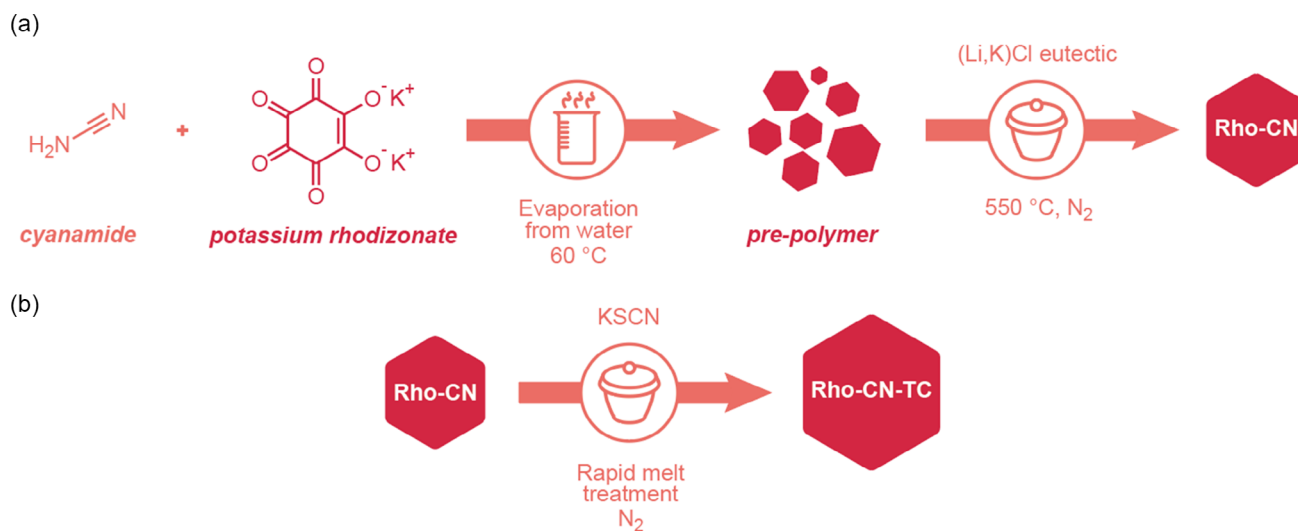

Figure 1. Synthesis of photocatalysts. a) Two-step synthesis of Rho-CN. b) Synthesis of Rho-CN-TC catalysts by KSCN melt treatment of Rho-CNs.
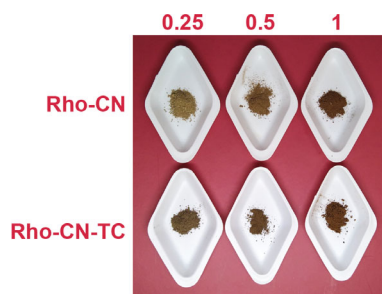
Figure 2. Appearance of Rho-CN-*X* and Rho-CN-TC-*X* catalysts, where *X* is the number indicating amount of K$_2$Rho in starting cyanamide–rhodizonate mixture (top line, in mol%).

were then characterized and tested in a series of photocatalytic experiments. The appearance of the materials is shown in **Figure 2**.

2.2. Characterization of Materials

2.2.1. Chemical Composition

The elemental composition of the synthesized materials is summarized in **Table 1**. The C/N ratio is lower than the theoretical value for perfectly condensed heptazine-based graphitic carbon nitride with the ideal composition of C$_3$N$_4$ (0.64), indicating doping with nitrogen. The increased nitrogen content can be attributed to large amount of terminal anionic –NCN groups at the surface or potential azo –N═N– bridges between units. Additionally, PTI materials tend to form hexagonal lattice where cavities form by absent triazine units that are occupied by alkaline metal chlorides, usually lithium chloride, and are often referred to as PTI/M$^+$Cl$^-$ (M = Li or K).[27] Indeed, inductively coupled plasma optical emission spectrometry (ICP-OES) results show combined metal content in the catalysts between 8.4% and 11.8% with lithium-to-potassium gram atomic ratio of about 3:1. This indicates a large fraction of anionic imide functions present in the materials, which is further increased by KSCN melt treatment: due to high concentration of potassium ions in the melt, some of the lithium ions are also replaced and washed off the material.

To further investigate structural composition of the catalysts, the samples were subjected to powder X-ray diffraction (PXRD)

Table 1. Chemical composition of synthesized materials.

Sample[a]	N [%]	C [%]	H [%]	S [%]	C/N [mass]	C/H [mass]	K [%]	Li [%]
Rho-CN-0.25	49.3	28.5	1.6	–	0.58	18.4	5.8	3.4
Rho-CN-0.5	47.4	27.6	2	–	0.58	13.8	5.6	3.4
Rho-CN-1	48.2	28.3	1.8	–	0.59	15.6	4.6	3.8
Rho-CN-TC-0.25	47.8	28.0	1.5	0.4	0.59	18.4	8.8	2.7
Rho-CN-TC-0.5	47.0	27.9	1.7	0.3	0.59	16.7	9.9	1.9
Rho-CN-TC-1	47.9	28.4	1.4	0.3	0.59	20.0	7.6	2.9

[a]Percentage of N, C, and H elements was obtained from combustion analysis. Percentage of K and Li was obtained from ICP-OES. Values given in mass percentages.
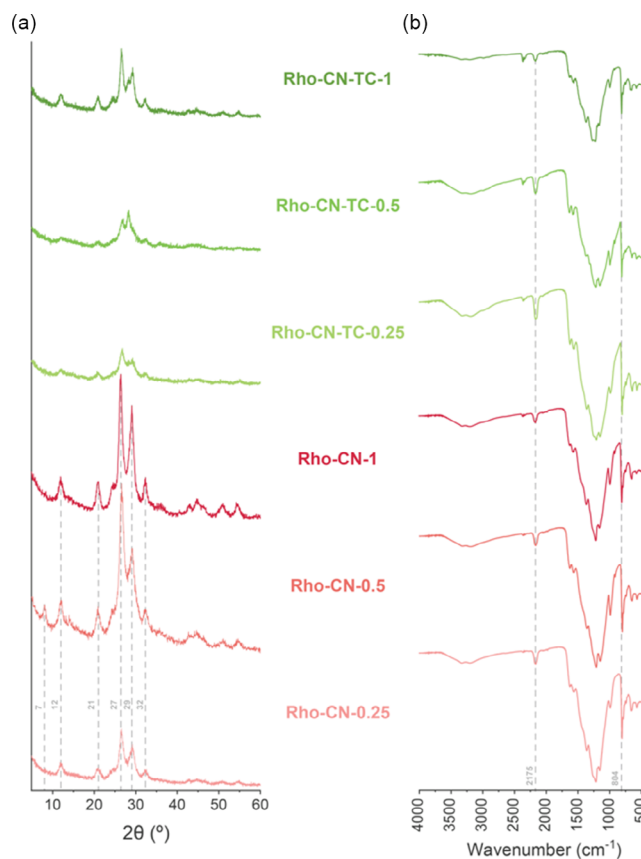

Figure 3. Phase and functional group characterization of the catalysts. a) PXRD patterns of Rho-CN and Rho-CN-TC materials. b) FT-IR spectra of Rho-CN and Rho-CN-TC materials.

analysis. As indicated by broad diffraction peaks, the synthesized materials are nanocrystalline (**Figure 3**a). Pronounced peaks at 12°, 21°, 24°, 29°, and 32° along with a series of peaks of low intensity at 40–55° are characteristic for PTI/Li$^+$Cl$^-$ phase.[27b,28] In the case of Rho-CN-0.5, the peak at 7–8° indicates the presence of potassium poly(heptazine imide) (K-PHI) phase.[25a,29] Therefore, addition of 0.5 mol% of potassium rhodizonate into cyanamide induces formation of a hybrid composite comprising PTI/Li$^+$Cl$^-$ and K-PHI phases. Additionally, the Rho-CN series demonstrates relatively high degree of crystallinity, while Rho-CN-TC catalysts are close to being amorphous, which is attributed to the decrease of PTI/Li$^+$Cl$^-$ crystallite size during KSCN melt treatment.

According to Fourier transform infrared (FT-IR) data, heptazine and triazine ring units' vibrations are located in the 1650–800 cm^{-1} region. The heptazine characteristic peak is observed at 804 cm^{-1}, while the peak at ≈2175 cm^{-1} corresponds to anionic cyanamide K-RNCN triple C≡N bond vibration (Figure 3b).[26]

X-ray photoelectron spectroscopy (XPS) studies were performed to obtain data on chemical composition from C, N, O, K, and Li bond regions (**Figure 4**a–d). Characteristic C$_{1s}$ carbon nitride peaks at 284.5 eV (C═C of adventitious carbon) and 287.9 eV (C═N–C of the ring) are present along with hydroxylated C–OH carbon at 288.1 eV[30]; however, the ratio between the two fits neither purely heptazine nor triazine imide phase with 288 eV peak being dominant for the latter.[31] This may
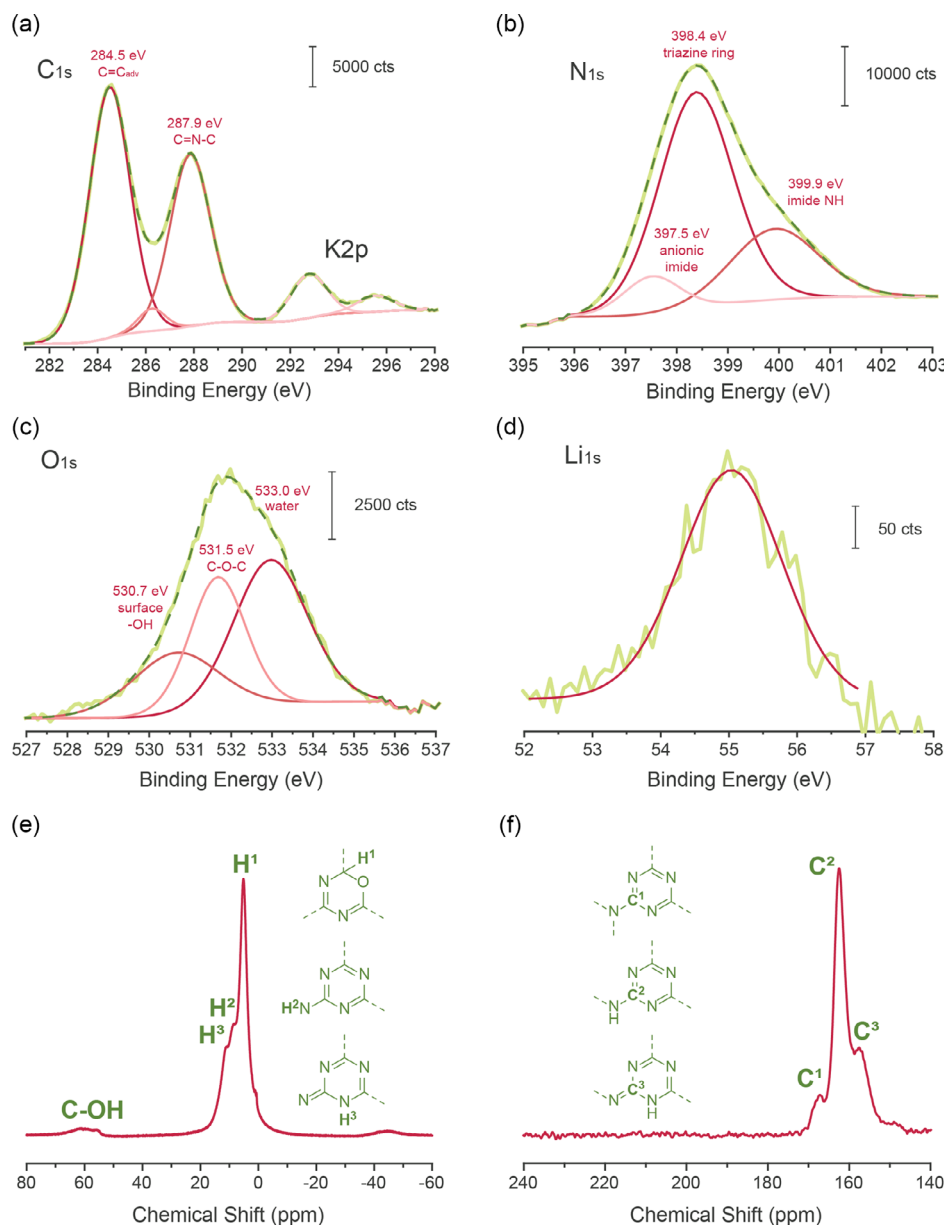
Figure 4. Characterization of Rho-CN-0.5 material: a) C_{1s} and K_{2p}, b) N_{1s}, c) O_{1s}, and d) Li_{1s} XPS spectra; bars indicate Y axis scale in counts. e) ^1H MAS and f) ^{13}C CP-MAS NMR spectra; chemical structures of heptazine units indicate different types of atoms and their respective signals according to the reference.[32]

indicate presence of PHI phase, which is supported by a small 1.8% atomic content of K^+ ions which characteristic peaks at 292.8 and 295.5 eV are also present. In N_{1s} region, typical signals of imide–NH bridges at 399.9 eV and triazine nitrogen at 398.4 eV are observed with a usual ratio of about 1:3. Additionally, a weaker peak at 397.5 eV is also present, which may be attributed to a deprotonated imide nitrogen that is characteristic for PHI phase. O_{1s} provides three contributions at 530.7 (surface –OH), 531.5 (C–O–C), and 533.0 eV (adsorbed water). Finally, Li_{1s} shows a characteristic 55 eV peak of Li^+ ion.

Proton and carbon magic angle spinning solid-state nuclear magnetic resonance (^1H MAS and ^{13}C CP-MAS NMR) spectra of Rho-CN-0.5 demonstrate predominance of the PTI/Li^+Cl^-

phase in the material, showing peaks at 5, 8, and 11 ppm in the proton and 157, 162, and 167 ppm in the carbon spectrum, respectively (Figure 4e,f).[32] No characteristic sharp heptazine carbon peaks at 155, 163, and 167 ppm were observed;[33] however, the heptazine fraction of the material is supposed to be minor, and its signals may be lost in noise during spectra accumulation due to heavy overlapping with those of PTI/Li^+Cl^-.

2.2.2. DRUV–vis and Fluorescence Spectroscopy

Electronic spectra in the ultraviolet and visible (UV–vis) range of Rho-CN and Rho-CN-TC samples acquired in diffuse reflectance

(DR) mode are shown in **Figure 5**a and feature several distinctive absorption bands: primary absorption at ≈450 nm, which is defined by electron transitions between the valence and conduction band, and onset of absorption at ≈750 nm. The latter, in the context of the theory of molecular orbitals, is usually ascribed to transitions between the nonbonding and antibonding molecular orbitals (n–π^* transitions).[34] By increasing the amount of K_2Rho in its mixture with cyanamide, the n–π^* transitions become more pronounced, which results in progressively increased absorption at wavelength >450 nm. The DRUV–vis plots were used to determine the optical bandgap of materials (see Figure S2, Supporting Information, for plots). Rho-CN-0.25 and Rho-CN-0.5 demonstrate similar bandgap values of 2.58 and 2.56 eV, respectively, which is slightly lower than the one reported for K-PHI (2.68 eV), shifting closer to the one of CN-OA-m (2.32 eV) poly(heptazine imide) catalysts.[25b] Treatment with KSCN slightly increases bandgap to 2.73 for the 0.25% catalyst, which may be attributed to etching of rhodizonate-induced defects in the salt melt, changes in morphology and crystallinity, or sulfur doping[35] (see Table 1). In general, the trend observed for both catalyst series is that higher concentration of K_2Rho decreases the bandgap by moving the valence band level to more negative values. Bandgaps and band positions are further discussed in the electrochemistry section.

Steady-state fluorescence spectra were acquired upon excitation of the samples at 410 nm (Figure 5b). All samples emit photons in the range 430–800 nm. Within a series of synthesized materials, emission spectra demonstrate several peaks at around 450, 575, and 675 nm. Intensity of these peaks progressively decreases with the concentration of potassium rhodizonate in the reaction mixture. For all samples with K_2Rho content of 1 mol%, the major emission peak is registered at 675 nm.

Furthermore, the overall fluorescence intensity progressively decreases as concentration of potassium rhodizonate in the reaction mixture increases from 0.25 to 1 mol%, which clearly indicates quenching of the radiative decay of excitons. The results of time-resolved emission spectroscopy indicate excitons that are characterized by the lifetime ≤20–60 ps relax via fluorescence. The low quantum yield of fluorescence suggests that radiative relaxation of the materials singlet excited state is not the only pathway for the recovery of the ground state and most likely includes singlet–triplet intersystem crossing (**Table 2**).[29a,36]

2.2.3. Electron Microscopy

The samples' morphology was studied using scanning electron microscopy (SEM) and transmission electron microscopy (TEM). As materials' surface features are consistent within their respective Rho-CN or Rho-CN-TC class, SEM images for

Table 2. Fluorescence lifetimes for synthesized materials.

Sample[a]	Fluorescence lifetime [ps]
Rho-CN-0.25	20.83 ± 0.75
Rho-CN-0.5	26.22 ± 2.25
Rho-CN-1	20.48 ± 1.67
Rho-CN-TC-0.25	59.09 ± 30.25
Rho-CN-TC-0.5	41.78 ± 9.77
Rho-CN-TC-1	29.63 ± 5.83

[a]Excitation wavelength: 375 nm; emission was detected at 550 nm. The decay curves were fitted using a nonlinear method with a multicomponent decay law.
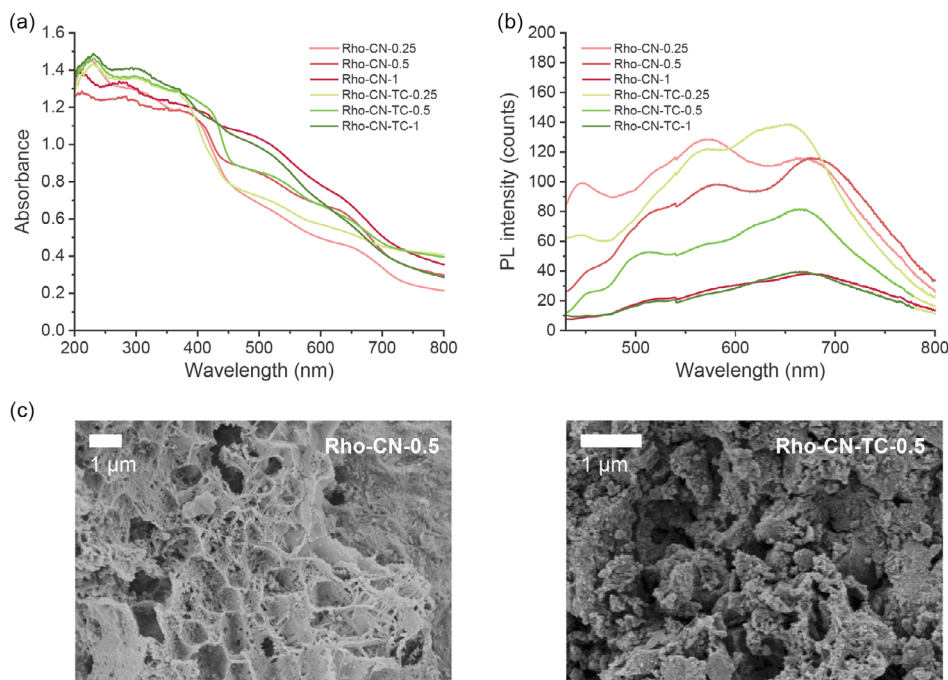

Figure 5. Spectroscopic and SEM characterization of Rho-CN and Rho-CN-TC catalysts. a) DRUV–vis absorption spectra of materials. b) Steady-state emission spectra of materials. c) SEM images showing the morphology of materials containing 0.5 mol% K_2Rho.

0.5 mol% of potassium rhodizonate samples are provided in Figure 5c as representative examples. As observed in Figure 5c, the 20–70 μm-sized particles of the Rho-CN series have macropores and cavities of 0.5–5 μm size on their surface, as well as some rectangular imprints from salt template crystals which were removed before by washing. Another feature of these materials is the presence of individual needle-shaped crystallites and their rectangular grid networks on surfaces, which could be attributed to the PTI/Li$^+$Cl$^-$ phase.[27b] Rho-CN-TC particles are generally smaller and have a coarser surface due to their etching with KSCN melt. Surface crystallites are also decreased in size, and needle-like structures are no longer present after treatment, which supports the crystallinity decrease provided by PXRD data.

TEM analysis confirmed the formation of two phases, which are strikingly different in morphology. The sample mostly consists of micrometer-sized flakes (**Figure 6**a). High-resolution images obtained from such flakes show numerous nanodomains (about 6 nm) which form a continuous network. Selected area electron diffraction patterns from these flakes and from individual domains in such flakes are indexed in an orthorhombic lattice with unit cell parameters $a = 14.38(14)$ Å, $b = 8.25(15)$ Å, $c = 6.70(2)$ Å (Figure 6d,b inset), typical for the PTI structure.[29a] A small amount of agglomerates that consist of needle-like crystallites belong to the second phase. Interplanar distances measured on HRTEM images (as, e.g., in Figure 6f) are equal to $d_{100} = 10.25$ Å, typical for the potassium polyheptazine imide structure.[29a] Overall, characterization data suggest that PTI/Li$^+$Cl$^-$ and PHI phases coexist, while the building units, i.e., triazines and heptazines, are interconnected at the interface between these two phases.

2.2.4. Electrochemistry

To investigate the electrochemical properties, cyclic voltammetry was performed on photoelectrodes prepared from Rho-CN and Rho-CN-TC with conductive Nafion binder in aqueous media (0.1 M Na$_2$SO$_4$, saturated silver chloride reference electrode), but no conclusive data on reduction and oxidation potentials values were extracted from the plots (Figure S7, Supporting Information). While Rho-CN in the dark shows a cathodic wave ranging from –0.20 V versus SHE for Rho-CN-0.5 to +0.21 V versus SHE for Rho-CN-0.25, the Rho-CN-TC catalyst shows almost uniform behavior providing the potential around –0.10 V versus
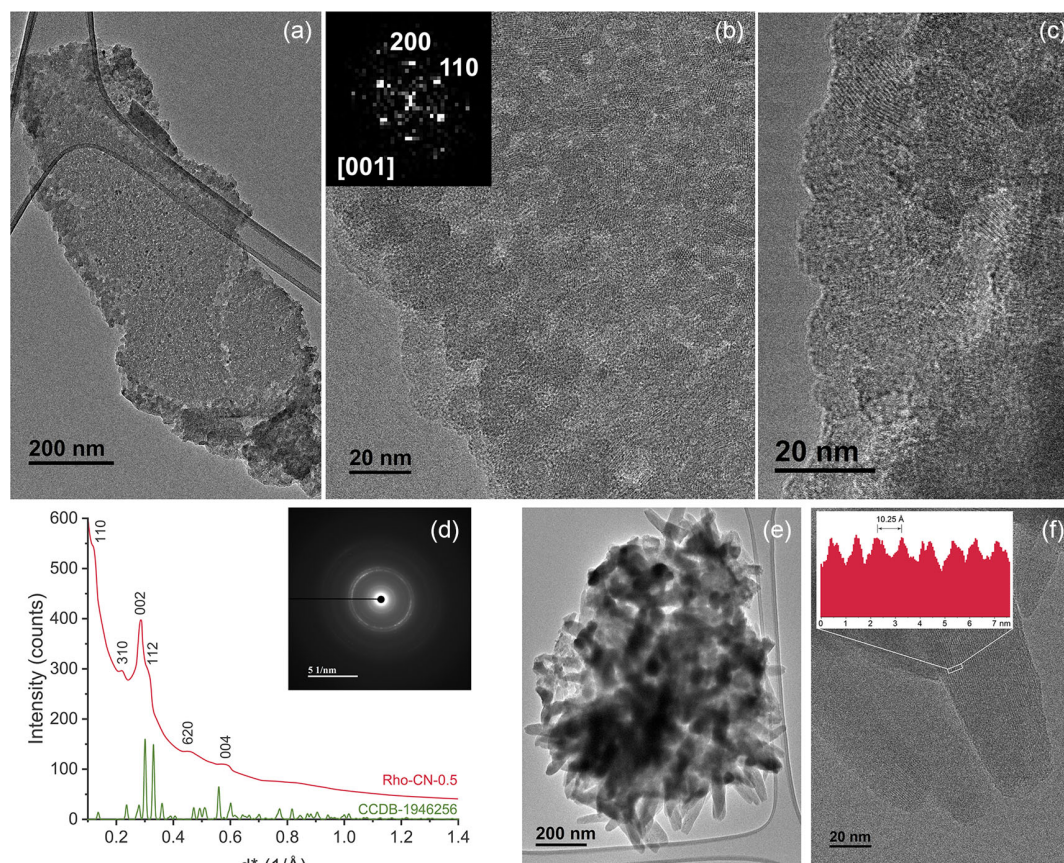

Figure 6. a) Low-magnification TEM image, showing typical morphology of the Rho-CN-0.5 sample; b,c) HRTEM images show that flat flakes consist of crystallites of about 6 nm in diameter; inset in (b) shows a fast Fourier transform indexed in the orthorhombic unit cell of PTI (CCDB-1946256),[27a] d) SAED pattern collected from PTI flakes; red: azimuthally averaged intensity profile obtained from the SAED pattern shown in inset; green: theoretical intensity profile obtained using CCDB-1946256 data for the PTI crystal structure. e) Low-magnification TEM image of the second phase in the sample. f) HRTEM image of individual crystals in (e) with simulated profile, the distance between lattice planes corresponds to $d_{100} = 10.25$ Å of the polyheptazine imide structure.[29a]

SHE. As expected, electrochemical stability of the samples increases with concentration of K_2Rho, which is evident by more stable current values during multiple scans (see Figure S7, Supporting Information, for CV plots).

Mott–Schottky analysis (Figure S6, Supporting Information) demonstrates an increase of K_2Rho content in Rho-CN to provide a more positive flatband potential in the range of −0.38 to −0.28 V versus SHE, whereas for Rho-CN-TC the trend is reversed (from −0.29 for 0.25% to −0.51 V vs SHE for 1%, respectively). Valence band values were then obtained by adding the optical bandgap values derived from DRUV–vis plots to the flatband potentials (**Figure 7**a). Compared to reported PHI-based and NCN-functionalized catalysts,[25b] the materials possess slightly more reductive power at the cost of oxidation potential due to narrowed bandgap, which may be useful for designing net-reductive photoredox processes.

Additionally, transient photocurrent response and electrochemical impedance spectra (EIS) were recorded. Typical photocurrent without sacrificial electron donor ranges at approximately 150–400 nA cm^{-2} with two outstanding examples of Rho-CN-0.5 and Rho-CN-TC-1 reaching ≈1.2 µA cm^{-2} during the first scan (Figure 7b, data for other samples are provided in Figure S8, Supporting Information), which may indicate an optimal concentration of conductive sites provided by K_2Rho dopant. EIS data for Rho-CN series are in good agreement with photocurrent values (Figure 7c for Rho-CN-0.5 and Rho-CN-TC-1 samples; plots for other photocatalysts are provided in Figure S9, Supporting Information) with the most conductive samples giving higher current. However, there is no such dependency in Rho-CN-TC series, presumably due to strong structural changes induced by melt treatment, which is supported by SEM imaging.

2.3. Photocatalytic Performance

2.3.1. Benzylamine Oxidation

Our investigation of photocatalytic properties of Rho-CN and Rho-CN-TC materials started with evaluating their ability to
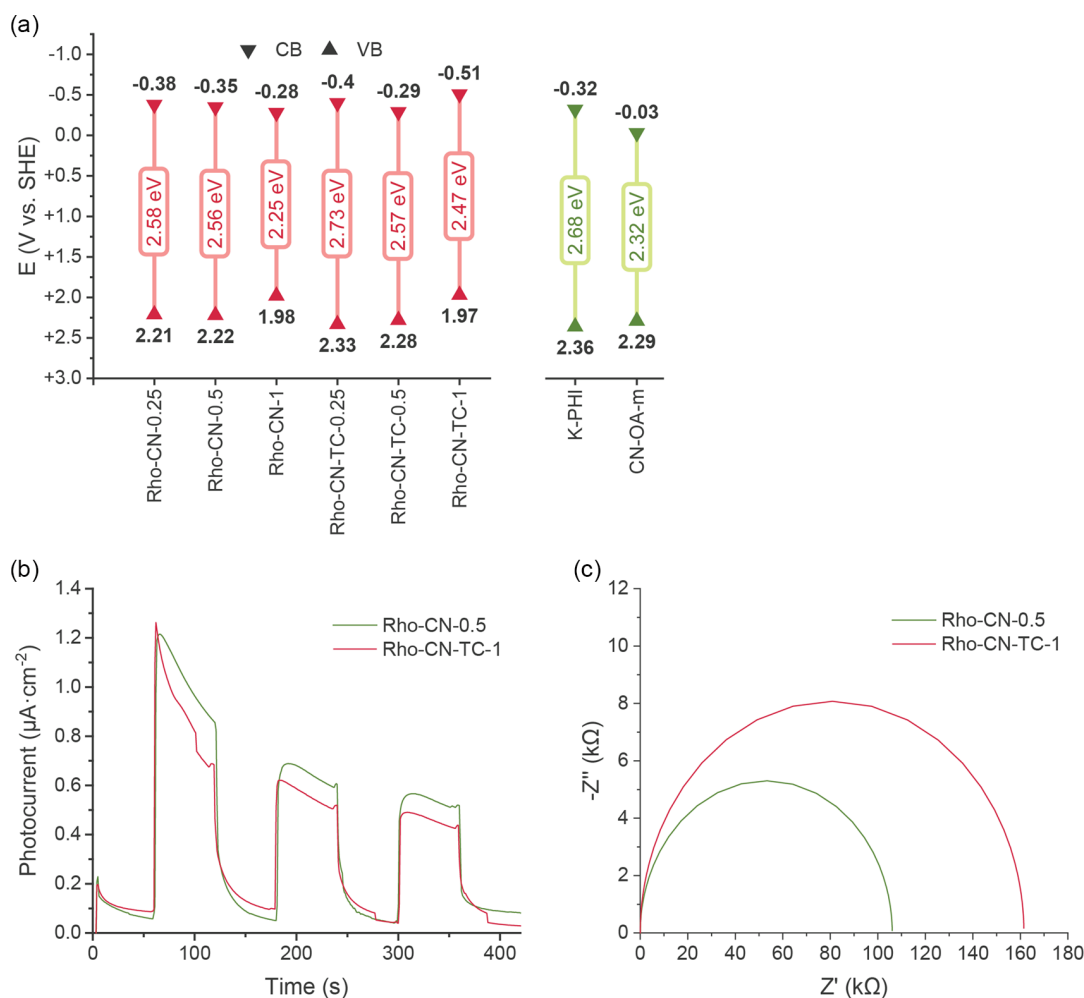

Figure 7. Electrochemical properties of photocatalysts. a) Band positions and bandgap values for Rho-CN and Rho-CN-TC materials versus SHE. CB values are the average value from 2 flatband potential measurements; optical bandgaps are derived from DRUV–vis plots. Comparison values of CB, VB, and bandgaps for K-PHI and CN-OA-m benchmark catalysts are sourced from reference.[25b] b) Transient photocurrent response of Rho-CN-0.5 and Rho-CN-TC-1 under white LED irradiation with 60 s light and 60 s dark cycles. c) Nyquist plots of potentiostatic EIS spectra of Rho-CN-0.5 and Rho-CN-TC-1.

operate under lower energy irradiation, given their relatively strong absorbance in the red region of the visible spectrum. As a model reaction, aerobic oxidation of benzylamine to *N*-benzyl-1-phenylmethanimine was chosen; this process is a commonly used benchmark to test the oxidative power of photocatalysts[37] because the model substrate has a relatively accessible oxidation potential of +1.04 V versus SCE (+1.28 V versus SHE) in acetonitrile.[38] The materials were irradiated under oxygen atmosphere in an acetonitrile solution of benzylamine along with two previously described highly anionic catalysts, K-PHI[39] and CN-OA-m,[40] used as references for comparison. The results of photocatalytic tests are shown in **Figure 8**a. In this reaction, Rho-CN-TC materials provide yields ranging from 65% to quantitative, which is comparable to the 97% obtained for CN-OA-m under the same wavelength.

Therefore, Rho-CN-TC catalysts outperform their parent Rho-CN materials (54–77%). In both sets of catalysts, the best results are achieved by the samples prepared from 0.5 mol% K_2Rho mixture, indicating the optimal amount of dopant agent. Performance of catalysts in this case may be attributed to several factors, as both direct oxidation of benzylamine by a carbon nitride or energy transfer (EnT) yielding reactive singlet oxygen can occur. However, the reactivity of CNs under longer wavelength irradiation is generally attributed to the predominance of an EnT process,[36,41] which may indicate better energy transfer and singlet oxygen generation by Rho-CN-TC series catalysts. Given a positive Stokes shift, absorption of photons with longer wavelength by Rho-CN-TC would give a less energetic excited state with better spectral overlap with the energy acceptor, in this case O_2.
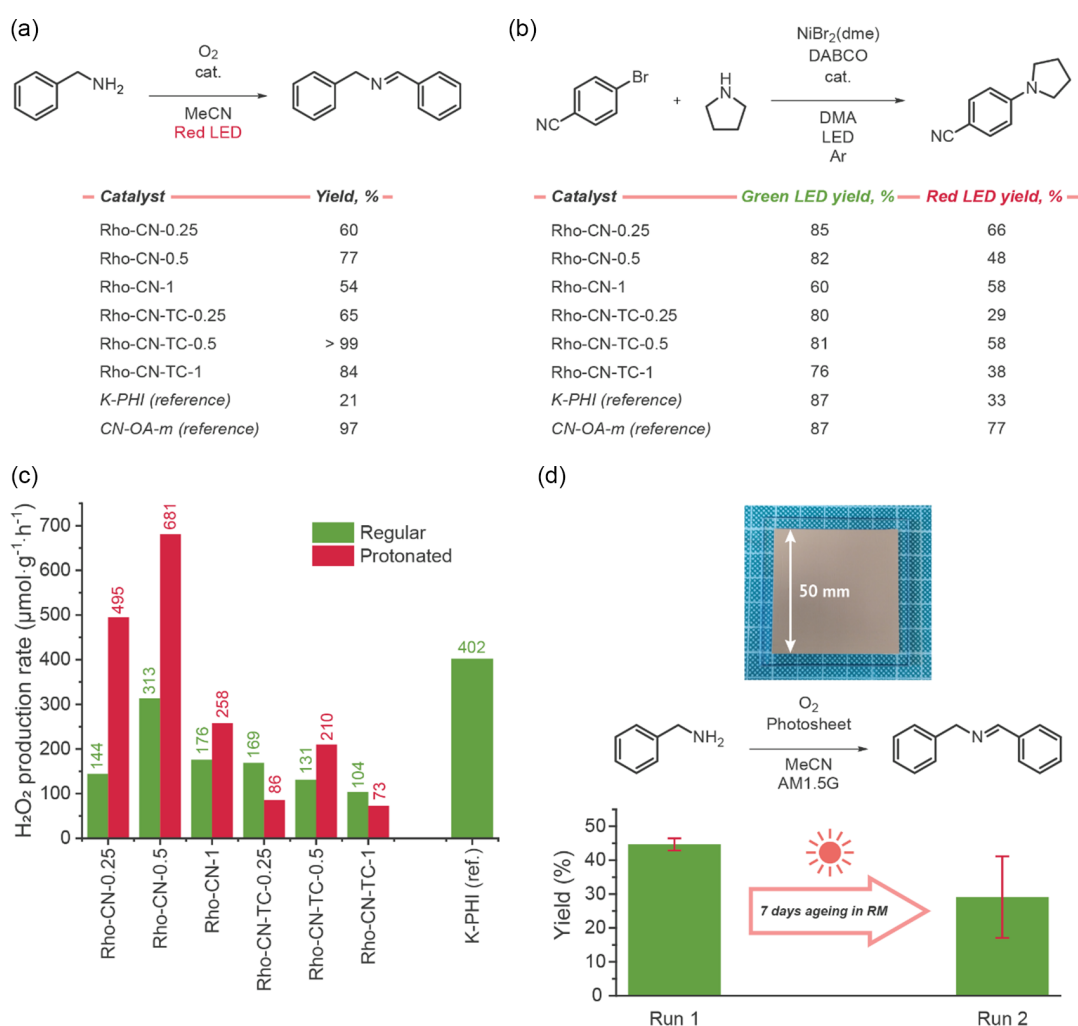

Figure 8. Photocatalytic performance of materials. a) Oxidation of benzylamine. Conditions: benzylamine (50 µmol), photocatalyst (5 mg), acetonitrile (2 mL); oxygen atmosphere introduced by purging the mixture for 60 s; yields are determined by GC–MS. b) Dual photoredox/nickel cross-coupling. Conditions: 4-bromobenzonitrile (200 µmol), pyrrolidine (1.8 equiv.), DABCO (2.2 equiv.), NiBr$_2$(dme) (5 mol%), catalyst (12 mg), *N,N*-dimethylacetamide (DMA, 1 mL), argon atmosphere. c) Hydrogen peroxide evolution. Conditions: catalyst (5 mg), water–methanol mixture (2 mL, 4:1 v/v), white LED; oxygen atmosphere introduced by purging the mixture for 60 s. d) Benzylamine oxidation experiment with ≈25 cm^2 photocatalytic sheet (top) in flow cell prepared from Rho-CN-0.5. Conditions: preoxygenated solution of benzylamine in acetonitrile (0.025 M), 1.6667 mL min^{-1} flow rate, 480 ± 10 s residence time. Graph (bottom) indicates yields of imine in 2 runs before and after ageing in reaction mixture determined by HPLC (DAD detector at 254 nm). See Supporting Information for detailed description of photocatalytic experiments.

2.3.2. Dual Photoredox/Nickel C–N Cross-Coupling

Palladium-catalyzed C–C and C-heteroatom cross-coupling reactions play an important role in general synthetic and discovery organic chemistry,[42] and a vast field of research is dedicated to developing more earth-abundant and cheap alternatives to precious metals. While nickel-based catalysts display generally lower performance to palladium due to a number of kinetics-related issues and poor availability of precatalysts,[43] coupling them with photocatalysts significantly speeds up their redox cycle by promoting the formation of active Ni(I) or Ni(0) species, which allows for compatible performance and the possibility to utilize Ni^{2+} precatalysts.[44] There are a number of publications proving carbon nitrides to be photoredox auxiliaries to nickel complexes in C–C, C–N, C–S, and C–O coupling reactions.[22,45] Therefore, we chose C–N cross-coupling between 4-bromobenzonitrile and pyrrolidine as our next model reaction to study the photocatalytic performance of the new materials. Again, K-PHI and CN-OA-m were selected as reference catalysts. The reaction was carried out either under green (530 nm) or red (625 nm)[46] LED irradiation to prevent metal catalyst losses as nickel black which is common under shorter wavelength light.[44] The results are shown in Figure 8b. Under green light, the samples demonstrated compatible performance to the reference catalysts, albeit being slightly inferior under irradiation with red light. Similar to benzylamine oxidation, the tendency for 0.5 mol% K_2Rho sample to demonstrate higher yields is somewhat preserved. However, Rho-CN-0.5 is the less active catalyst of Rho-CN series under 625 nm despite having higher absorption at this wavelength than Rho-CN-0.25.

2.3.3. Hydrogen Peroxide Evolution

Hydrogen peroxide is a valuable and atom-efficient bulk oxidizer; however, the main method of its production relies on sequential cycle of reduction and autooxidation of anthraquinones catalyzed by palladium.[47] The main drawbacks of this process are the necessity for large amounts of organic "carrier" and hazardous hydrogen gas used in the reduction step, thus raising demand for cheap, safe, and fast method for production. The extensive research on this topic includes electrochemical[48] and photocatalytic[49] processes using cheap bulk chemicals as sacrificial donors. To test the ability of our materials to produce hydrogen peroxide upon O_2 reduction, we carried out the reaction in 4:1 v/v mixture of water and methanol, which served as a sacrificial donor of electrons for the catalysts. The H_2O_2 content was measured after 1 h of irradiation photometrically by formation of complex with titanium(IV) oxysulfate. K-PHI was used as a benchmark catalyst, providing 402 μmol g^{-1} h^{-1} of hydrogen peroxide. The results are shown in Figure 8c. As well as in organic transformation, the trend for 0.5 mol% K_2Rho samples is observed in hydrogen peroxide evolution (HPE) reaction with Rho-CN-0.5 providing 313 μmol g^{-1} h^{-1} of peroxide. Rho-CN-TC series demonstrates marginally worse performance. As it is reported that low pH increases photocatalytic peroxide production,[50] and considering our highly anionic samples should provide plenty of local acidic sites after protonation, catalysts H-Rho-CNs and H-Rho-CN-TCs were prepared by treating the samples

with 3 M HCl solution and then tested in the reaction as well. Indeed, despite noticeable discoloration of the catalysts, their activity increased more than twofold up to 681 μmol g^{-1} h^{-1} in the case of H-Rho-CN-0.5.

2.3.4. Flow Photosheet Performance

Previous experiments demonstrate that, among two series of catalysts, Rho-CN-0.5 possesses an optimal balance between performance and cost efficiency and thus is a more "universal" catalyst than others. To demonstrate the scalability and recyclability of our catalysts, a "photosheet" device[51] was assembled by blade-coating 50 × 50 mm area of a smooth glass panel with ≈50–55 μm-thick layer of Rho-CN-0.5 (Figure 8d). The photosheet was then assembled into a 50 × 50 × 10 mm³ flow cell with a transparent window and studied for the benzylamine oxidation reaction (0.025 M in acetonitrile solution was used) under irradiation by an AM1.5G solar simulator to emulate outdoor conditions for possible scale-up applications. In 8 min residence time, the catalytic layer was able to provide 44.7 ± 1.8% yield. To test the stability and reusability, the photosheet cell was irradiated over the course of 7 days (168 h) filled with oxygenated concentrated benzylamine solution in acetonitrile, and then tested in flow mode again using 0.025 M solution. The yield decreased to 29.1 ± 12.0%, indicating a certain degree of catalyst degradation, which is confirmed visually by slight discoloration of the catalyst (see Figure S1c, Supporting Information, for comparison). The mechanical integrity of the catalytic layer remained unchanged even after multiple runs and cell washings, which demonstrates the potential for fabrication of large working surface devices.

2.3.5. Miscellaneous Reactions

Hydrogen Evolution: According to previous results, we chose Rho-CN-0.5 as a model catalyst for hydrogen evolution reaction (HER), as well as its protonated version, H-Rho-CN-0.5. Both materials were used as is, in addition to the samples with pre-deposited nickel phosphide (Ni_2P) and metallic platinum cocatalysts with ethylene glycol (EG) and triethanolamine (TEOA) being used as sacrificial electron donors in basic aqueous media (self-provided basicity in case of TEOA and KOH in case of EG); finally, in the last pair of samples platinum was photodeposited in situ. Reaction was performed under AM1.5G solar simulator. Unfortunately, only traces of hydrogen at the limit of device detection were observed in case of Ni_2P cocatalyst present; some amount was also produced by samples with in situ photodeposition of platinum, which is likely coming from the deposition step itself. Both EG and TEOA are shown to be sufficient electron donors for the catalysts based on significant color change from shades of brown to deep green, which was observed previously for electron–proton pair storage of K-PHI carbon nitride.[52] The reason behind the low performance for HER may be due to insufficient overpotential created by its conductive band, which is −0.35 V versus SHE (see CV data above), resulting in inability to provide the cocatalyst with enough energy for successful proton reduction to occur. Here, see Supporting Information for experimental details.

Table 3. Summary of properties and photocatalytic activity of the materials.

Catalyst	CB versus SHE [V]	VB versus SHE [V]	Fluorescence lifetime [ps]	Hydrogen peroxide evolution [μmol g^{-1} h^{-1}]$^{a)}$	Benzylamine oxidation yield [%]	Cross-coupling yield [%]$^{b)}$
Rho-CN-0.25	−0.38	2.21	20.83 ± 0.75	144 (495)	60	85 (66)
Rho-CN-0.5	−0.35	2.22	26.22 ± 2.25	313 (681)	77	82 (48)
Rho-CN-1	−0.28	1.98	20.48 ± 1.67	176 (258)	54	60 (58)
Rho-CN-TC-0.25	−0.40	2.33	59.09 ± 30.25	169 (86)	65	80 (29)
Rho-CN-TC-0.5	−0.29	2.28	41.78 ± 9.77	131 (210)	>99	81 (58)
Rho-CN-TC-1	−0.51	1.97	29.63 ± 5.83	104 (73)	84	76 (38)

$^{a)}$Values in parentheses indicate production for protonated catalyst; $^{b)}$Yields are given for green LED; values in parentheses represent red LED yields.

Chromoselectivity: Previously, our group discovered a reaction of *S*-arylthioacetates oxidation in the presence of aqueous HCl with K-PHI photocatalyst.[13b] The selectivity of this reaction depends heavily on the light source used, providing corresponding aryl chlorides under 365 nm UV light, arylsulfonyl chlorides under 465 nm blue light, and diaryl disulfides under longer wavelengths (≥530 nm), respectively. Considering the strong absorption >450 nm, we tested the performance of Rho-CN and Rho-CN-TC catalysts in the oxidation of *S*-acetylthiophenol under irradiation at 530 nm. Thus, under irradiation with green light, Rho-CN-0.5 gave diphenyl disulfide with >95% selectivity, while for K-PHI the selectivity toward this product was 68%. The main side product in both cases was *S*-phenyl benzenesulfonothioate.

Interestingly, upon irradiation of a reaction mixture containing Rho-CN-TC-1 at 465 nm the major product was *S*-phenyl benzenesulfonothioate (49% yield) while diphenyl disulfide was observed as a minor side product (7%). Considering nearly identical potentials of the bands edges for all catalysts of Rho-CN-TC series, this result points to unusual catalytic behavior where multistep S-oxidation is seemingly more kinetically favorable than the single-electron formation of active chlorine species from HCl. This feature may be utilized further in photoredox reaction design to shift the selectivity of known processes toward desired multielectron processes.

Combination of high-throughput synthesis with statistical analysis is a powerful approach to designing photocatalytically active materials.[53,54] From the summary shown in **Table 3**, it is clear that there is no a single photocatalyst that performs equally well in all processes. By applying statistical analysis to the whole dataset, we found the CB potential correlates weakly with the yield of cross-coupling product obtained under irradiation with red light (Table S3, Supporting Information). On the other hand, the VB potential correlates weakly with the yield of cross-coupling product under irradiation with green light. Such results might be explained by the change of the mechanism from electron transfer under green light (driving force for the photoinduced electron transfer is the decisive factor) to energy transfer under red light (better spectral overlap between a sensitizer excited state and energy acceptor).[46] Fluorescence lifetime alone does not show strong correlation with any of the parameters, which is due to low fluorescence quantum efficiency—radiative relaxation of the excited state is not a dominant pathway for the recovery of the ground state. However, a stronger correlation exists between the product of the CB potential and the fluorescence lifetime and the yield of cross-coupling product under red light (Table S4, Supporting Information). Nevertheless, in all cases, correlation coefficients are significantly lower than ±1, suggesting the influence of other properties of the catalysts on their performance. These properties are, for example, the interface between PTI/Li$^+$Cl$^-$ and K-PHI phases, which is difficult to quantify with a single value.

On the other hand, by considering datasets for Rho-CN and Rho-CN-TC separately, stronger correlations between materials properties and their performance in the selected reaction were found (Table S5–S8, Supporting Information). As can be seen from Table S5, Supporting Information, yields of net-oxidative benzylamine transformation enabled by Rho-CN photocatalysts correlate with the VB potential and fluorescence lifetime. Similar correlation is noted between hydrogen peroxide production and fluorescence lifetime. Under green light, more negative CB potential values provide greater yields in dual photoredox/nickel C–N cross-coupling, which is likely due to facilitated Ni(II) to Ni(I) reduction.[55] On the other hand, more positive VB potential values correlate with the yields in dual photoredox/nickel C–N cross-coupling, which points at alternative mechanism involving oxidation of Ni(II) to Ni(III).[56] Overall, by tuning band position and PL lifetime by changing K$_2$Rho/cyanamide ratio, desired performance in a selected process can be achieved.

3. Conclusion

Using a multistep approach, we synthesized novel ionic Rho-CN carbon nitride materials with high absorption throughout the visible range and multiphase structure based primarily on PTI/Li$^+$Cl$^-$ with unique morphology. Due to the inexpensiveness and availability of reagents, as well as high yields of final materials and their comparable performance (Table S9, Supporting Information), Rho-CNs and Rho-CN-TCs were found to be cost-effective and potentially competitive to known PHI-based carbon nitride materials in lab scale and beyond, as demonstrated by the experiment using a Rho-CN-coated 50 × 50 mm photocatalytic sheet. The optimal fraction of potassium rhodizonate additive was evaluated to be 0.5 mol%, as indicated by multiple photocatalytic reactions. Additional potassium thiocyanate rapid melt posttreatment of Rho-CN catalysts provided the

Rho-CN-TC series, which possesses even higher light absorption and thus enhanced performance in net-oxidative reactions. However, improvements in dual nickel catalysis were found to be negligible. These sets of experiments demonstrate the versatility and high tunability of cyanamide–rhodizonate platform to yield photocatalysts for desired applications.

Supporting Information

Supporting Information is available from the Wiley Online Library or from the author.

Conflict of Interest

A patent WO/2019/081036 has been filed by Max Planck Gesellschaft zur Förderung der Wissenschaften E.V. in which O.S. and M.A. are listed as co-authors.

Data Availability Statement

The data that support the findings of this study are available from the corresponding author upon reasonable request.

[1] A. Savateev, I. Ghosh, B. König, M. Antonietti, *Angew. Chem., Int. Ed. Engl.* **2018**, *57*, 15936.

[2] a) A. Savateev, M. Antonietti, *ChemCatChem* **2019**, *11*, 6166; b) T. S. Miller, A. B. Jorge, T. M. Suter, A. Sella, F. Cora, P. F. McMillan, *Phys. Chem. Chem. Phys.* **2017**, *19*, 15613.

[3] A. Thomas, A. Fischer, F. Goettmann, M. Antonietti, J.-O. Müller, R. Schlögl, J. M. Carlsson, *J. Mater. Chem.* **2008**, *18*, 4893.

[4] X. Wang, K. Maeda, A. Thomas, K. Takanabe, G. Xin, J. M. Carlsson, K. Domen, M. Antonietti, *Nat. Mater.* **2009**, *8*, 76.

[5] S. Cao, J. Low, J. Yu, M. Jaroniec, *Adv. Mater.* **2015**, *27*, 2150.

[6] L. Jiang, X. Yuan, Y. Pan, J. Liang, G. Zeng, Z. Wu, H. Wang, *Appl. Catal., B* **2017**, *217*, 388.

[7] G. Zhang, L. Lin, G. Li, Y. Zhang, A. Savateev, S. Zafeiratos, X. Wang, M. Antonietti, *Angew. Chem., Int. Ed. Engl.* **2018**, *57*, 9372.

[8] D. Liu, C. Li, C. Zhao, Q. Zhao, T. Niu, L. Pan, P. Xu, F. Zhang, W. Wu, T. Ni, *Chem. Eng. J.* **2022**, *438*, 135623.

[9] T. Ni, H. Zhang, Z. Yang, L. Zhou, L. Pan, C. Li, Z. Yang, D. Liu, *J. Colloid Interface Sci.* **2022**, *625*, 466.

[10] D. Liu, C. Li, T. Ni, R. Gao, J. Ge, F. Zhang, W. Wu, J. Li, Q. Zhao, *Appl. Surf. Sci.* **2021**, *555*, 149677.

[11] Y. Markushyna, C. A. Smith, A. Savateev, *Eur. J. Org. Chem.* **2019**, *2020*, 1294.

[12] a) V. W. Lau, D. Klose, H. Kasap, F. Podjaski, M. C. Pignie, E. Reisner, G. Jeschke, B. V. Lotsch, *Angew. Chem., Int. Ed. Engl.* **2017**, *56*, 510; b) S. Mazzanti, C. Schritt, K. ten Brummelhuis, M. Antonietti, A. Savateev, *Exploration* **2021**, *1*, 20210063.

[13] a) L. Schmermund, S. Reischauer, S. Bierbaumer, C. K. Winkler, A. Diaz-Rodriguez, L. J. Edwards, S. Kara, T. Mielke, J. Cartwright, G. Grogan, B. Pieber, W. Kroutil, *Angew. Chem., Int. Ed. Engl.* **2021**, *60*, 6965; b) Y. Markushyna, C. M. Schusslbauer, T. Ullrich, D. M. Guldi, M. Antonietti, A. Savateev, *Angew. Chem., Int. Ed. Engl.* **2021**, *60*, 20543.

[14] a) A. Galushchinskiy, Y. Zou, J. Odutola, P. Nikacevic, J. W. Shi, N. Tkachenko, N. Lopez, P. Farras, O. Savateev, *Angew. Chem., Int. Ed. Engl.* **2023**, *62*, e202301815; b) A. J. Rieth, Y. Qin, B. C. M. Martindale, D. G. Nocera, *J. Am. Chem. Soc.* **2021**, *143*, 4646.

[15] T. Botari, W. P. Huhn, V. W.-H. Lau, B. V. Lotsch, V. Blum, *Chem. Mater.* **2017**, *29*, 4445.

[16] A. M. Beale, A. L. Craigmill, S. Wetzlich, *Arch. Environ. Contam. Toxicol.* **1991**, *20*, 423.

[17] G. Iraci, M. H. Back, *Can. J. Chem.* **1988**, *66*, 1293.

[18] Potassium rhodizonate, technical, 85%, CAS RN: 13021-40-4; 392340; Aldrich, Sigma Aldrich, Taufkirchen, Germany, April **2022**, https://www.sigmaaldrich.com/DE/en/sds/aldrich/392340 (accessed: November 2022).

[19] P. W. Preisler, L. Berger, *J. Am. Chem. Soc.* **1942**, *64*, 67.

[20] M. Lee, J. Hong, J. Lopez, Y. Sun, D. Feng, K. Lim, W. C. Chueh, M. F. Toney, Y. Cui, Z. Bao, *Nat. Energy* **2017**, *2*, 861.

[21] B. Eistert, H. Fink, H.-K. Werner, *Liebigs Ann. Chem.* **1962**, *657*, 131.

[22] I. Ghosh, J. Khamrai, A. Savateev, N. Shlapakov, M. Antonietti, B. König, *Science* **2019**, *365*, 360.

[23] T. Güthner, B. Mertschenk, *Ullmann's Encyclopedia of Industrial Chemistry*, John Wiley & Sons, Inc. **2006**, 645–667.

[24] N. Fechler, N. P. Zussblatt, R. Rothe, R. Schlögl, M. G. Willinger, B. F. Chmelka, M. Antonietti, *Adv. Mater.* **2016**, *28*, 1287.

[25] a) H. Schlomberg, J. Kroger, G. Savasci, M. W. Terban, S. Bette, I. Moudrakovski, V. Duppel, F. Podjaski, R. Siegel, J. Senker, R. E. Dinnebier, C. Ochsenfeld, B. V. Lotsch, *Chem. Mater.* **2019**, *31*, 7478; b) I. F. Teixeira, N. V. Tarakina, I. F. Silva, G. A. Atta Diab, N. L. Salas, A. Savateev, M. Antonietti, *J. Mater. Chem. A* **2022**, *10*, 18156.

[26] V. W. Lau, I. Moudrakovski, T. Botari, S. Weinberger, M. B. Mesch, V. Duppel, J. Senker, V. Blum, B. V. Lotsch, *Nat. Commun.* **2016**, *7*, 12165.

[27] a) C. Z. Liao, V. W. Lau, M. Su, S. Ma, C. Liu, C. K. Chang, H. S. Sheu, J. Zhang, K. Shih, *Inorg. Chem.* **2019**, *58*, 15880; b) E. Wirnhier, M. Doblinger, D. Gunzelmann, J. Senker, B. V. Lotsch, W. Schnick, *Chem. Eur. J.* **2011**, *17*, 3213.

[28] S. Mazzanti, A. Savateev, *ChemPlusChem* **2020**, *85*, 2499.

[29] a) A. Savateev, N. V. Tarakina, V. Strauss, T. Hussain, K. Ten Brummelhuis, J. M. Sanchez Vadillo, Y. Markushyna, S. Mazzanti, A. P. Tyutyunnik, R. Walczak, M. Oschatz, D. M. Guldi, A. Karton, M. Antonietti, *Angew. Chem., Int. Ed. Engl.* **2020**, *59*, 15061; b) Z. Chen, A. Savateev, S. Pronkin, V. Papaefthimiou, C. Wolff,

M. G. Willinger, E. Willinger, D. Neher, M. Antonietti, D. Dontsova, *Adv. Mater.* **2017**, *29*, 1700555.

[30] D. Dontsova, S. Pronkin, M. Wehle, Z. Chen, C. Fettkenhauer, G. Clavel, M. Antonietti, *Chem. Mater.* **2015**, *27*, 5170.

[31] D. Burmeister, H. A. Tran, J. Muller, M. Guerrini, C. Cocchi, J. Plaickner, Z. Kochovski, E. J. W. List-Kratochvil, M. J. Bojdys, *Angew. Chem., Int. Ed. Engl.* **2022**, *61*, e202111749.

[32] M. B. Mesch, K. Barwinkel, Y. Krysiak, C. Martineau, F. Taulelle, R. B. Neder, U. Kolb, J. Senker, *Chem. Eur. J.* **2016**, *22*, 16878.

[33] Z. Jin, X. Jiang, Q. Zhang, S. Huang, L. Zhang, L. Huang, T. He, H. Zhang, T. Ohno, S. Ruan, Y.-J. Zeng, *Commun. Mater.* **2020**, *1*, 104252.

[34] G. Zhang, A. Savateev, Y. Zhao, L. Li, M. Antonietti, *J. Mater. Chem. A* **2017**, *5*, 12723.

[35] H. Lv, Y. Huang, R. T. Koodali, G. Liu, Y. Zeng, Q. Meng, M. Yuan, *ACS Appl. Mater. Interfaces* **2020**, *12*, 12656.

[36] A. Galushchinskiy, K. Brummelhuis, M. Antonietti, A. Savateev, *ChemPhotoChem* **2021**, *5*, 1020.

[37] a) M. Chandra, U. Guharoy, D. Pradhan, *ACS Appl. Mater. Interfaces* **2022**, *14*, 22122; b) S. Wei, H. Zhong, H. Wang, Y. Song, C. Jia, M. Anpo, L. Wu, *Appl. Catal., B* **2022**, *305*, 121032; c) Z. Su, B. Zhang, X. Cheng, M. Xu, G. Chen, Y. Sha, Y. Wang, J. Hu, R. Duan, J. Zhang, *Dalton Trans.* **2022**, *51*, 13601.

[38] S. P. M. Ung, I. Perepichka, C. J. Li, *Helv. Chim. Acta* **2021**, *105*, e202100190.

[39] A. Savateev, D. Dontsova, B. Kurpil, M. Antonietti, *J. Catal.* **2017**, *350*, 203.

[40] G. Zhang, G. Li, Z. A. Lan, L. Lin, A. Savateev, T. Heil, S. Zafeiratos, X. Wang, M. Antonietti, *Angew. Chem., Int. Ed. Engl.* **2017**, *56*, 13445.

[41] H. Wang, S. Jiang, S. Chen, D. Li, X. Zhang, W. Shao, X. Sun, J. Xie, Z. Zhao, Q. Zhang, Y. Tian, Y. Xie, *Adv. Mater.* **2016**, *28*, 6940.

[42] a) A. Biffis, P. Centomo, A. Del Zotto, M. Zecca, *Chem. Rev.* **2018**, *118*, 2249; b) P. Ruiz-Castillo, S. L. Buchwald, *Chem. Rev.* **2016**, *116*, 12564; c) C. C. Johansson Seechurn, M. O. Kitching, T. J. Colacot, V. Snieckus, *Angew. Chem., Int. Ed. Engl.* **2012**, *51*, 5062.

[43] A. K. Cooper, P. M. Burton, D. J. Nelson, *Synthesis* **2019**, *52*, 565.

[44] S. Gisbertz, S. Reischauer, B. Pieber, *Nat. Catal.* **2020**, *3*, 611.

[45] a) C. Cavedon, A. Madani, P. H. Seeberger, B. Pieber, *Org. Lett.* **2019**, *21*, 5331; b) B. Pieber, J. A. Malik, C. Cavedon, S. Gisbertz, A. Savateev, D. Cruz, T. Heil, G. Zhang, P. H. Seeberger, *Angew. Chem., Int. Ed. Engl.* **2019**, *58*, 9575.

[46] Y. Zou, S. Abednatanzi, P. Gohari Derakhshandeh, S. Mazzanti, C. M. Schusslbauer, D. Cruz, P. Van Der Voort, J. W. Shi, M. Antonietti, D. M. Guldi, A. Savateev, *Nat. Commun.* **2022**, *13*, 2171.

[47] J. M. Campos-Martin, G. Blanco-Brieva, J. L. Fierro, *Angew. Chem., Int. Ed. Engl.* **2006**, *45*, 6962.

[48] X. Shi, S. Siahrostami, G. L. Li, Y. Zhang, P. Chakthranont, F. Studt, T. F. Jaramillo, X. Zheng, J. K. Norskov, *Nat. Commun.* **2017**, *8*, 701.

[49] a) J. Liu, Y. Zou, B. Jin, K. Zhang, J. H. Park, *ACS Energy Lett.* **2019**, *4*, 3018; b) H. Hou, X. Zeng, X. Zhang, *Angew. Chem., Int. Ed. Engl.* **2020**, *59*, 17356.

[50] a) M. Teranishi, S.-I. Naya, H. Tada, *J. Phys. Chem. C* **2016**, *120*, 1083; b) M. Gryszel, M. Sytnyk, M. Jakesova, R. Romanazzi, R. Gabrielsson, W. Heiss, E. D. Glowacki, *ACS Appl. Mater. Interfaces* **2018**, *10*, 13253.

[51] T. Uekert, M. A. Bajada, T. Schubert, C. M. Pichler, E. Reisner, *ChemSusChem* **2021**, *14*, 4190.

[52] Y. Markushyna, P. Lamagni, C. Teutloff, J. Catalano, N. Lock, G. Zhang, M. Antonietti, A. Savateev, *J. Mater. Chem. A* **2019**, *7*, 24771.

[53] X. Li, P. M. Maffettone, Y. Che, T. Liu, L. Chen, A. I. Cooper, *Chem. Sci.* **2021**, *12*, 10742.

[54] S. Vijayakrishnan, J. W. Ward, A. I. Cooper, *ACS Catal.* **2022**, *12*, 10057.

[55] Y. Qin, B. C. M. Martindale, R. Sun, A. J. Rieth, D. G. Nocera, *Chem. Sci.* **2020**, *11*, 7456.

[56] C. Zhu, H. Yue, J. Jia, M. Rueping, *Angew. Chem., Int. Ed.* **2021**, *60*, 17810.